





# Origin of the Excess of High-energy Retrograde Stars in the Galactic Halo

Tadafumi Matsuno<sup>1,2</sup> , Wako Aoki<sup>1,2</sup> , and Takuma Suda<sup>3</sup> <sup>1</sup> Department of Astronomical Science, School of Physical Sciences, SOKENDAI (The Graduate University for Advanced Studies), Mitaka, Tokyo 181-8588, Japan  
tadafumi.matsuno@nao.ac.jp<sup>2</sup> National Astronomical Observatory of Japan (NAOJ), 2-21-1 Osawa, Mitaka, Tokyo 181-8588, Japan<sup>3</sup> Research Center for the Early Universe, The University of Tokyo, 7-3-1 Hongo, Bunkyo-ku, Tokyo 113-0033, Japan

Received 2018 September 10; revised 2019 March 5; accepted 2019 March 11; published 2019 April 8

## Abstract

We report on the very low  $\alpha$ -element abundances of a group of metal-poor stars with high orbital energy and with large retrograde motion in the Milky Way halo, whose excess has been reported recently from metallicity and kinematics. We constructed a sample of halo stars with measured abundances and precise kinematics, including  $\sim 880$  stars with  $[\text{Fe}/\text{H}] < -0.7$ , by crossmatching the Stellar Abundances for Galactic Archaeology database to the second data release of *Gaia*. Three regions in the energy-angular momentum space have been selected: the innermost halo, *Gaia* Enceladus/Sausage, and the high-energy retrograde halo. While the innermost halo and *Gaia* Enceladus regions have chemical abundances consistent with high- and low- $\alpha$  populations in the halo, respectively, chemical abundances of stars in the high-energy retrograde halo are different from the two populations; their  $[\text{X}/\text{Fe}]$ , where X represents Na, Mg, and Ca, are even lower than those in *Gaia* Enceladus. These abundances, as well as their low mean metallicity, provide a new support for the idea that the retrograde component is dominated by an accreted dwarf galaxy which has a longer star formation timescale and is less massive than *Gaia* Enceladus/Sausage.

**Key words:** Galaxy: abundances – Galaxy: halo – Galaxy: kinematics and dynamics – Galaxy: stellar content – Galaxy: structure

## 1. Introduction

One of the current goals of astronomy is to reconstruct the formation history of the Milky Way. To this end, signatures of past galaxy accretions are extensively searched for from photometric observations (e.g., Ibata et al. 1994; Belokurov et al. 2006; Grillmair 2006; Bernard et al. 2016) and stellar kinematic information (e.g., Helmi et al. 1999, 2017; Klement et al. 2009; Smith et al. 2009; Myeong et al. 2018a) in the Galactic halo. However, it may be difficult to identify a single accretion event from stellar kinematics alone (Jean-Baptiste et al. 2017). Therefore, combining chemical and kinematic information is of paramount importance, as the chemical abundances of stars can differ from system to system, for example among dwarf galaxies (Tolstoy et al. 2009).

There have been suggestions of the existence of two components among Galactic halo stars both in kinematics and chemical abundances (e.g., Chiba & Beers 2000; Carollo et al. 2007; Nissen & Schuster 2010). Further detailed investigations were realized thanks to precise measurements of stellar positions, distances, and proper motions by the *Gaia* mission (Gaia Collaboration et al. 2016b). A number of studies now draw a consistent picture using *Gaia* Data Release 1 (Gaia Collaboration et al. 2016a) and 2 (Gaia Collaboration et al. 2018; Lindegren et al. 2018) that there is a large population of halo stars that show highly eccentric orbits with modest retrograde motion and low- $\alpha$  element abundances, and that they were brought to the Milky Way halo through an accretion of a single massive dwarf galaxy, which is called the *Gaia* Sausage/*Gaia* Enceladus (e.g., Belokurov et al. 2018; Deason et al. 2018; Haywood et al. 2018; Helmi et al. 2018; Koppelman et al. 2018; Myeong et al. 2018b; see also an independent result by Kruijssen et al. 2018).

A next step is to investigate if we can find other clear accretion signatures. Helmi et al. (2017) and Myeong et al. (2018c) pointed out the excess of stars with high-energy and retrograde orbits using

astrometric information from the *Gaia* data (Helmi et al. 2017), and astrometric and metallicity information from the combination of *Gaia* and the Sloan Digital Sky Survey (Myeong et al. 2018c). This excess might be related to a study in the pre-*Gaia* era, which showed that stars with large retrograde motion have low  $\alpha$ -element abundances (Stephens & Boesgaard 2002; Venn et al. 2004). This possible connection should be investigated with the recent astrometric measurements by *Gaia* and with a large sample of metal-poor stars whose abundances have been measured from high-resolution spectra.

The chemical abundances of  $>1000$  metal-poor stars have been revealed by continuous efforts to identify such stars and measure their stellar abundances. These abundances are compiled in the Stellar Abundances for Galactic Archaeology (SAGA) database (Suda et al. 2008, 2011; Yamada et al. 2013; Suda et al. 2017).

We investigated the current chemo-kinematic view of the stellar halo by combining the SAGA database and *Gaia* DR2. In this Letter, we report a new evidence for a past accretion event (e.g., Venn et al. 2004; Myeong et al. 2018c), confirming its extragalactic origin and strengthening the case that it differs from the *Gaia* Sausage/Enceladus. This feature is prominent at low metallicity ( $[\text{Fe}/\text{H}] \lesssim -1.5$ ) and has very low  $\alpha$ -element abundances within the range of  $-2.0 \lesssim [\text{Fe}/\text{H}] \lesssim -1.5$ , with large retrograde motion. After describing the sample selection process in Section 2, we present results in Section 3. Discussions are presented in Section 4.

## 2. Sample

### 2.1. The SAGA Database

#### 2.1.1. Chemical Abundances

The abundances of metal-poor stars were extracted from the SAGA database. This database compiles abundances of

metal-poor stars from studies that used high- or medium-resolution spectrographs ( $R \gtrsim 7000$ ). Given that the density of metal-poor stars on the sky is very low, high-resolution spectroscopic surveys using multi-object spectrographs are not efficient. Therefore, the use of the SAGA database is an efficient way to obtain chemical abundances of many elements for a large number of metal-poor stars. We started with  $\sim 2100$  metal-poor stars ( $[\text{Fe}/\text{H}] < -0.7$ ) in this database.

Since our study is based on the abundance data collected from literature, we take two major sources of abundance uncertainties in the SAGA database into consideration. One is caused by different methods of abundance analyses among different studies, for example, different stellar parameters or different line lists. The other is that we mixed various types of stars from main-sequence stars to red giants, between which there could be offsets in abundances caused, e.g., by departures from the local thermo-dynamic equilibrium and plane-parallel approximations in real stellar photospheres (non-local thermal equilibrium (NLTE)/3D effects). Hereafter, we denote  $\sigma_1$  and  $\sigma_2$  to indicate the contribution from the first and the second effect, respectively. The total uncertainty  $\sigma$  can be expressed as  $\sigma^2 = \sigma_1^2 + \sigma_2^2$ . We note that uncertainties from the literature are not explicitly adopted in the error estimate here because these uncertainties should be included in the  $\sigma$  values evaluated by the following procedure.

In the following assessments of the uncertainties, we used all of the stars in the database that have  $-3.0 < [\text{Fe}/\text{H}] < -2.5$  and those have  $-2 < [\text{Fe}/\text{H}] < -1$ . The  $\sigma$  values are expressed as  $\sigma_{\text{mp}}$  and  $\sigma_{\text{mr}}$  for the former and the latter sample, respectively. As seen below, our focus in this Letter is the metallicity range of  $-2 < [\text{Fe}/\text{H}] < -1$ , and hence  $\sigma_{\text{mr}}$  matters. The  $\sigma_1$  was assessed by investigating the median value of the standard deviations of the abundance measurements for individual objects for which more than two studies had reported abundances. The  $\sigma_{1,\text{mp}}$  values (numbers of stars used) are  $0.18^{+0.06}_{-0.04}$  (20),  $0.13^{+0.05}_{-0.03}$  (42),  $0.08^{+0.02}_{-0.03}$  (35),  $0.16^{+0.07}_{-0.04}$  (43), and  $0.10^{+0.08}_{-0.02}$  (103) for [Na/Fe], [Mg/Fe], [Ca/Fe], [Ba/Fe], and [Fe/H], respectively, and the  $\sigma_{1,\text{mr}}$  are  $0.07^{+0.05}_{-0.02}$  (79),  $0.10^{+0.03}_{-0.04}$  (97),  $0.06^{+0.03}_{-0.02}$  (90),  $0.18^{+0.04}_{-0.04}$  (90), and  $0.10^{+0.04}_{-0.04}$  (196). The superscript and subscript indicate the values between the third quartile and the median and that between the median and the first quartile, respectively. We also directly evaluated  $\sigma_{\text{mp}}$  by examining a spread of [X/Fe] for each element with the assumption that intrinsic abundance spreads are smaller than the measurement errors at  $-3 < [\text{Fe}/\text{H}] < -2.5$ .<sup>4</sup> We conducted a linear regression and took the half of the difference between the 16th and 84th percentiles of residuals as  $\sigma_{\text{mp}}$ . The  $\sigma_{\text{mp}}$  values (numbers of stars used) are 0.31 (96), 0.13 (312), and 0.11 (310) for Na, Mg, and Ca.<sup>5</sup> Note that  $\sigma_{\text{mp}}$  evaluated by this process reflects both two sources of uncertainties. Thus it is possible to calculate  $\sigma_{2,\text{mp}}$  from the equation  $\sigma_{\text{mp}}^2 = \sigma_{1,\text{mp}}^2 + \sigma_{2,\text{mp}}^2$  as  $\sigma_{2,\text{mp}} = 0.25, 0.00, 0.08$ , respectively.<sup>6</sup> Assuming  $\sigma_2$  does not depend on metallicity (i.e.,  $\sigma_{2,\text{mp}} = \sigma_{2,\text{mr}}$ ), we get  $\sigma_{\text{mr}} = 0.27, 0.10$ , and  $0.10$  for [Na/Fe],

[Mg/Fe], and [Ca/Fe].<sup>7</sup> Since there is no way to estimate  $\sigma_{\text{mp}}$  for [Fe/H] and thus  $\sigma_{2,\text{mp}}$  and  $\sigma_{2,\text{mr}}$ , we assumed  $\sigma_{\text{mr}} = 1.5 \times \sigma_{1,\text{mr}} = 0.15$  without estimating the  $\sigma_2$  values. It is also not possible to estimate  $\sigma_{\text{mp}}$  for [Ba/Fe] due to the intrinsic abundance spread at low metallicity. Therefore, we again skipped the estimation of  $\sigma_2$  and assume  $\sigma_{\text{mr}} = 0.27$  for [Ba/Fe]. The estimated errors are small enough not to significantly affect our conclusions.

The systematic uncertainties of abundances among different papers are discussed in Suda et al. (2008) where they picked up 17 stars having multiple measurements for carbon abundances and compared their offsets for the stellar parameters and abundances (see their Figure 10). Possible causes of the uncertainties are also listed, while the inconsistency by the use of different solar abundances from paper to paper is alleviated by the update of the database as discussed in Suda et al. (2017).

### 2.1.2. Positions, Distances, and Proper Motions

Stellar positions and proper motions were obtained from *Gaia* DR2. Here, we briefly explain the process of cross-matching the SAGA database to *Gaia* DR2. The details of the method will be presented in a forthcoming paper.

We complemented incomplete stellar position data in the database from Simbad using star names and inspected 2MASS images (Cutri et al. 2003) to examine the accuracy of the positions. After manually correcting the coordinates as required, the SAGA database was crossmatched to 2MASS using the coordinates. Most of the stars are sufficiently bright to be detected by 2MASS. Finally, astrometric information was obtained via the `gaiadr2.tmass_best_neighbour` catalog. Twenty-five relatively faint stars have no counterparts in the 2MASS point-source catalog. We searched for these 25 objects directly in the `gaiadr2.gaia_source` catalog and visually checked the results using Pan-STARRS images. With a few exceptions, the SAGA database was successfully crossmatched with *Gaia* DR2. We plan to update the SAGA database to include *Gaia* information, as well as the kinematics of metal-poor stars. We adopted the distance estimates of Bailer-Jones et al. (2018) and further restricted the sample to stars with a `parallax_over_error > 5`. We also imposed an additional criterion using the equation C.1 of Lindegren et al. (2018). After these processes, 1571 metal-poor stars remained.

### 2.1.3. Radial Velocities

To obtain radial velocities, three sources were combined, *Gaia* DR2, the SAGA database, and Simbad, as none of them alone provided radial velocities for a sufficient number of stars. Radial velocities in the SAGA database and Simbad are based on past measurements in the literature; thus, these sources have heterogeneous data quality. The consistency among sources was evaluated by comparing their radial velocity values with those reported in *Gaia* DR2. Radial velocity data from the SAGA database were consistent with the measurements obtained by *Gaia* DR2 at the 2–3 km s<sup>-1</sup> level; those obtained from Simbad showed similar consistency when using values of quality A or B.

<sup>4</sup> This is not feasible for the metal-rich sample, since abundance ratios are sensitive to the timescale of star formation.

<sup>5</sup> We use stars with  $-2.5 < [\text{Fe}/\text{H}] < -2.0$  to measure  $\sigma_{\text{mp}}$  for Na since there is a population of extremely metal-poor stars that show very large Na enhancement.

<sup>6</sup> The above estimate results in a  $\sigma_{1,\text{mp}}$  value comparable to  $\sigma_{\text{mp}}$  for [Mg/Fe]. We interpret  $\sigma_2$  as negligible for [Mg/Fe] and consider  $\sigma_{2,\text{mr}} = 0$ . This would be because of similar ionization potentials of neutral Mg and Fe.

<sup>7</sup> The large metallicity dependence of  $\sigma_1$  for [Na/Fe] is probably because Na abundance measurements have to rely on the D lines at low metallicity, which are sensitive to the NLTE effect.  $\sigma_2$  is also expected to be smaller for high-metallicity stars and  $\sigma_{\text{mr}}$  for [Na/Fe] is likely to be overestimated.

We established priority in the order of *Gaia* DR2, the SAGA database, and Simbad. We excluded stars that showed significant radial velocity differences ( $>10 \text{ km s}^{-1}$  corresponding to  $\sim 3\sigma$ ) between different sources; most of them are considered to be in binary systems. As a result, we were left with 1290 metal-poor stars that showed no distinct radial velocity variation with good parallax measurements.

### 2.1.4. Kinematics

We used `galpy` (Bovy 2015) to calculate the kinematics of the stars. We first removed disk stars by applying  $\|v - v_{\text{LSR}}\| > 180 \text{ km s}^{-1}$ . As a result, we have 882 stars, among which 50% are within 0.88 kpc and 75% are within 2.07 kpc.

Energy ( $E$ ) and angular momentum ( $L_z$ ) were calculated adopting a modified `MWPotential2014` as the Milky Way gravitational potential (Bovy 2015). We replaced the relatively shallow Navarro–Frenk–White (NFW) potential in the `MWPotential2014` with the one with a virial mass of  $M_{200} = 1.4 \times 10^{12} M_{\odot}$ . The concentration parameter was also changed to  $c = 8.25$  to match the rotation curve of the Milky Way (K. Hattori 2018, private communication). We subtracted the potential energy at a very large distance from the obtained  $E$  to get  $E = 0$  at an infinite distance from the Galactic center, as explained in the document of `galpy`. The obtained  $E$ - $L_z$  distribution is presented in Figure 1.

### 2.2. LAMOST DR4

Since the number of stars in the database is still not very large and since there is a clear bias toward metal-poor stars in the database, we also investigate the  $E$ - $L_z$  distribution of metal-poor A-, F-, G-, and K-type stars cataloged in LAMOST DR4 (Cui et al. 2012, lower panel of Figure 1). We simply crossmatched stars in LAMOST estimated to be  $[\text{Fe}/\text{H}] < -0.7$  to *Gaia* DR2, and selected halo stars with the same criteria as those used for the SAGA database stars. We have 35,069 stars from LAMOST, and 50% of the stars are within 1.75 kpc and 75% are within 2.63 kpc. We just used these LAMOST stars to confirm the  $E - L_z$  distribution of stars in the SAGA database and to investigate the metallicity distributions of the selected regions.

### 2.3. Selection Boxes

In Figure 1, we show the distribution of stars with  $[\text{Fe}/\text{H}] < -0.7$  in the SAGA database in the  $E$ - $L_z$  plane. The contour was made using a Gaussian kernel density estimator. The upper panels show that the stellar kinematic properties vary with metallicity. At higher metallicity ( $[\text{Fe}/\text{H}] > -1.5$ ; upper left panel), we see the signature of *Gaia* Enceladus/Sausage at  $L_z \sim -500 \text{ kpc km s}^{-1}$  and  $E > -1.6 \times 10^5 \text{ km}^2 \text{ s}^{-2}$  (Belokurov et al. 2018; Deason et al. 2018; Haywood et al. 2018; Helmi et al. 2018; Koppelman et al. 2018; Myeong et al. 2018b). *Gaia* Enceladus is interpreted as the result of dwarf galaxy accretion. As we move toward lower metallicity ( $[\text{Fe}/\text{H}] < -1.5$ ), the *Gaia* Enceladus signature becomes weak (Belokurov et al. 2018; Myeong et al. 2018c). Instead, we see a clear enhancement of stars with retrograde motion. This metallicity difference between *Gaia* Enceladus and high-energy retrograde halo stars seems consistent with Figure 2 of Myeong et al. (2018c), who noted that the excess of high-energy retrograde stars extends down to  $[\text{Fe}/\text{H}] \sim -1.9$ , while the diamond shape in the  $L_z$ - $E$  space, corresponding to *Gaia* Sausage/Enceladus, extends down to  $[\text{Fe}/\text{H}] \sim -1.5$ .

The star distributions in LAMOST DR4 are similar to those in the SAGA database; the basic picture described above was confirmed by the LAMOST DR4 sample. Slight differences are attributable to the small number of stars in the SAGA database, the different metallicity distributions between the two samples, and/or the radial velocity and metallicity measurement quality. The SAGA database focuses on lower metallicity and has smaller uncertainties in radial velocity and metallicity measurements.

In the following chemical analysis, we compare the abundances of stars in the four regions in the  $E$ - $L_z$  plane, shown by the rectangles in Figure 1 (see also Table 1). The first three regions in  $E$ - $L_z$  are the innermost halo with small  $E$  and prograde motion (orange; labeled as A), *Gaia* Enceladus with high  $E$  and low  $L_z$  (cyan; B), and the high-energy retrograde stars (purple; C). The selection box C roughly corresponds to S1, Rg2, Rg3, Rg4, and Rg6 of Myeong et al. (2018d).<sup>8</sup> The last region, with a high  $E$  and prograde motion, was selected for the region C comparison (black; D). We note that results presented below are unchanged if we change the boundary  $L_z$  by a few  $\times 100 \text{ kpc km s}^{-1}$  or  $E$  by  $\sim 10^4 \text{ km}^2 \text{ s}^{-2}$  of the selection boxes.

## 3. Results

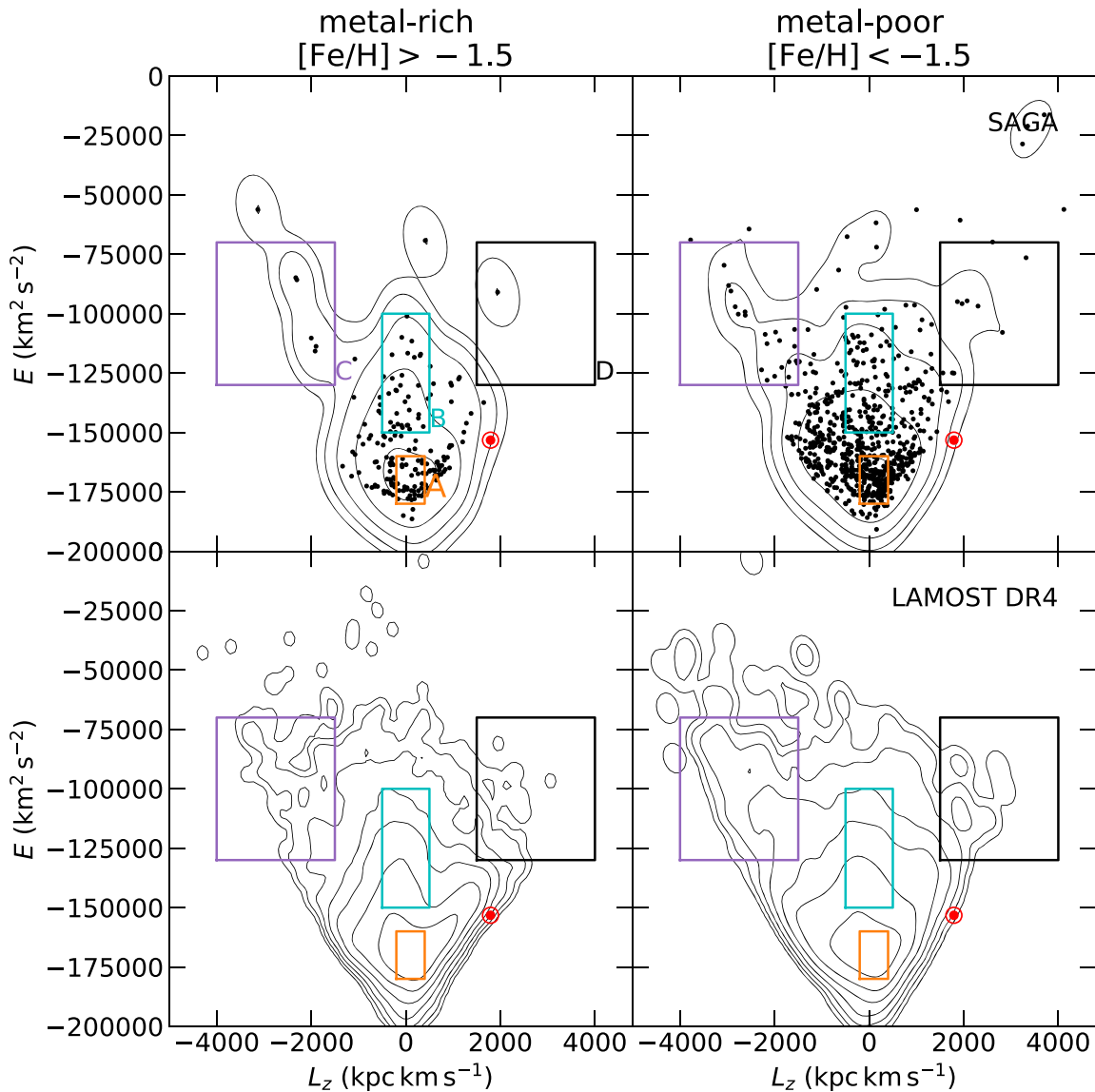
Figure 2 shows the metallicity distributions of the stars in the three regions from the LAMOST DR4 catalog. It is very clear that the three regions (A–C) have different metallicity distributions. The innermost halo (A) has the highest metallicity, while the retrograde substructure (C) has the lowest. In addition to this metallicity difference, we investigated abundance trends in detail in the following.

Figure 3 shows the chemical abundance trends of stars in the four regions for Na, Mg, Ca, and Ba from the SAGA database; notably, data points that had only upper limits were excluded. This did not affect Na, Mg, and Ca at  $[\text{Fe}/\text{H}] > -3.0$  and only one star belonging to the innermost region was excluded ( $[\text{Fe}/\text{H}] = -2.56$  and  $[\text{Ba}/\text{Fe}] < -1.32$ ). When a star had multiple measurements for a given element, we simply took the average of the values for plotting.

It is known that there are two distinct chemical populations in the Galactic halo, namely high-/low- $\alpha$  populations (e.g., Nissen & Schuster 2010). Nissen & Schuster (2010, 2011) showed that the high- $\alpha$  population has higher  $[\text{X}/\text{Fe}]$  for the three elements, Na, Mg, and Ca. Recent analyses of halo stars successfully associated the low- $\alpha$  population with the *Gaia* Enceladus from the kinematics and chemical abundances of stars (e.g., Haywood et al. 2018; Helmi et al. 2018). This chemical abundance difference is understood as a result from slower star formation in the low- $\alpha$  population. This slower star formation leads to lower metallicity by the time of onset of type Ia supernovae.

Figure 3 confirms lower  $\alpha$  abundances of *Gaia* Enceladus (B) relative to the innermost halo population (A). A striking feature shown in the figure is that the retrograde substructure (C) does not follow either of the overall abundance trends of *Gaia* Enceladus or that of the innermost halo, with even lower  $[\text{X}/\text{Fe}]$  of the three elements on average than those of *Gaia* Enceladus at  $[\text{Fe}/\text{H}] \gtrsim -2.0$ . This indicates that the retrograde

<sup>8</sup> Since our analysis and that of Myeong et al. (2018d) are different, the comparison is not very precise. However, we note that we obtain similar  $L_z$  and  $E$  for  $\omega$  Centauri ( $-595 \text{ kpc km s}^{-1}$ ,  $-1.78 \times 10^5 \text{ km}^2 \text{ s}^{-2}$ ) to their values ( $-496 \text{ kpc km s}^{-1}$ ,  $-1.85 \times 10^5 \text{ km}^2 \text{ s}^{-2}$ ).



**Figure 1.** Distribution of stars in the energy ( $E$ )—angular momentum ( $L_z$ ) space after dividing by the metallicity,  $[\text{Fe}/\text{H}] = -1.5$ , for stars in the SAGA database (upper panels) and in A-, F-, G-, and K-type stars cataloged in LAMOST DR4 (lower panels). Individual stars in the SAGA database are plotted, as well as the contour; for LAMOST stars, only the contour is shown. The rectangles show the four regions used in subsequent chemical analyses (Table 1). The location of the Sun is also shown by the red circles.

halo has a progenitor that is independent of the innermost halo or *Gaia* Enceladus. We further discuss the properties of the high-energy retrograde halo stars in the next section from the perspective of chemical abundance.

Region D was selected for the comparison. It has the same range of  $E$  as high-energy retrograde halo stars, but with prograde motion. Therefore, region D provides us with estimates of the contribution of the smooth component of the halo to region C. Region D does not have many stars at  $[\text{Fe}/\text{H}] > -2.5$  as region C, and a few stars with  $[\text{Fe}/\text{H}] > -2.5$  have different abundances from most of the stars in region C. This indicates that the high-energy retrograde halo stars cluster in both kinematic (Myeong et al. 2018c, 2018d) and chemical space and represents a distinct population.

For completeness, note that although we investigated other elements (C, Ti, Zn, Sr, Y, Ba, and Eu), we did not see significant differences among the regions, with Zn being an

exception such that it might show a hint of possible abundance difference between high-energy retrograde stars and *Gaia* Enceladus. Although the lack of a difference may be partially due to insufficient precision of the measured abundances, intrinsic abundance scatter of neutron captures elements, and/or abundance changes during the stellar evolution, Ba anomaly such as seen in  $\omega$  Centauri (Norris & Da Costa 1995) is clearly absent among the high-energy retrograde stars (lower right panel of Figure 3).

#### 4. Discussion

We approximated Mg and Ca abundance trends with the following form of function for the chemical evolution (Figures 3 and 4),

$$f(x) = \begin{cases} y_0 & (x < x_t) \\ a(x - x_t) + y_0 & (x > x_t) \end{cases}, \quad (1)$$



**Table 1**  
Properties of the Four Selected Regions

Region ID	Name	Number of Stars		$\langle L_z \rangle \pm \sigma_{L_z}$		$\langle E \rangle \pm \sigma_E$		$\langle [\text{Fe}/\text{H}] \rangle \pm \sigma_{[\text{Fe}/\text{H}]}$ LAMOST
		SAGA	LAMOST	SAGA $\times 10^3 \text{ kpc km s}^{-1}$	LAMOST $\times 10^3 \text{ kpc km s}^{-1}$	SAGA $\times 10^5 \text{ km}^2 \text{ s}^{-2}$	LAMOST $\times 10^5 \text{ km}^2 \text{ s}^{-2}$	
A	Innermost halo	161	8954	$0.10 \pm 0.17$	$0.12 \pm 0.17$	$-1.71 \pm 0.05$	$-1.70 \pm 0.05$	$-1.16 \pm 0.38$
B	<i>Gaia</i> Enceladus	135	4222	$-0.02 \pm 0.27$	$-0.06 \pm 0.26$	$-1.34 \pm 0.13$	$-1.36 \pm 0.11$	$-1.32 \pm 0.33$
C	high- <i>E</i> retrograde	26	299	$-2.17 \pm 0.48$	$-2.20 \pm 0.52$	$-1.08 \pm 0.14$	$-1.06 \pm 0.15$	$-1.60 \pm 0.33$
D	...	10	70	$2.14 \pm 0.54$	$1.93 \pm 0.35$	$-1.03 \pm 0.17$	$-1.14 \pm 0.12$	$-1.46 \pm 0.47$

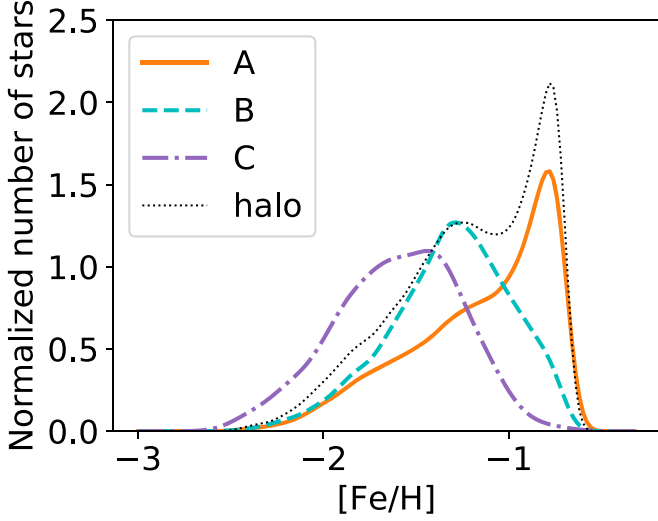


**Figure 2.** Normalized metallicity distribution functions of stars in the three selected regions and that of all the halo stars. This figure was constructed with a Gaussian kernel density estimator using the A-, F-, G-, and K-type stars cataloged in LAMOST DR4, without the SAGA database. Note that the sharp cutoffs at high metallicity are due to our sample selection with  $[\text{Fe}/\text{H}] < -0.7$  and that the histogram for the entire halo is multiplied by 1.5 for the purpose of visualization.

where  $x$  and  $y$  are for  $[\text{Fe}/\text{H}]$  and  $[\text{X}/\text{Fe}]$ , respectively. To obtain the set of parameters that describes the data best, we adopted the following likelihood,

$$p = \Pi_i \int f(\xi | [\text{Fe}/\text{H}]_i, \sigma_{[\text{Fe}/\text{H}]}) g([\text{X}/\text{Fe}]_i | \xi, \mathbf{x}) d\xi, \quad (2)$$

where

$$f = \frac{1}{\sqrt{2\pi\sigma_{[\text{Fe}/\text{H}]}}^2} \exp\left(-\frac{(\xi - [\text{Fe}/\text{H}]_i)^2}{2\sigma_{[\text{Fe}/\text{H}]}}\right) \quad (3)$$

$$g = (1 - f_o) \frac{1}{\sqrt{2\pi\sigma_{[\text{X}/\text{Fe}]}}^2} \exp\left(-\frac{([\text{X}/\text{Fe}]_i - f(\xi))^2}{2\sigma_{[\text{X}/\text{Fe}]}}\right) + f_o \frac{1}{\sqrt{2\pi(\sigma_{[\text{X}/\text{Fe}]}}^2 + \sigma_b^2)}} \exp\left(-\frac{([\text{X}/\text{Fe}]_i - \mu_b)^2}{2(\sigma_{[\text{X}/\text{Fe}]}}^2 + \sigma_b^2)}\right), \quad (4)$$

where  $f_o$ ,  $\mu_b$ , and  $\sigma_b$  are outlier fraction, mean, and standard deviation for the outlying population. We estimated a set of parameters,  $(a, x_t, \sigma_{[\text{X}/\text{Fe}]}, f_o, \mu_b, \sigma_b)$ , using a Markov chain Monte Carlo (MCMC) sampling while fixing  $y_0$  and  $\sigma_{[\text{Fe}/\text{H}]}$ . The mean  $[\text{X}/\text{Fe}]$  in  $-3.0 < [\text{Fe}/\text{H}] < -2.5$  were adopted as

$y_0$  (0.37 for Mg and 0.38 for Ca) and  $\sigma_{[\text{Fe}/\text{H}]} = 0.15$  was adopted. Flat priors with sufficiently wide ranges were adopted for the parameters except for  $x_t$  ( $-3 < x_t < -1$ ) and  $f_0$  ( $0 < f_0 < 0.5$ ).

Posterior distributions for  $a$  and  $x_t$  are shown in the lower panels of Figure 4. The posterior distributions show that *Gaia* Enceladus and high-energy retrograde stars are fit with different sets of parameters. The  $\sigma_X$  result is comparable to the estimated errors ( $\sigma_{[\text{Mg}/\text{Fe}]} = 0.12, 0.11, \text{ and } 0.12$  and  $\sigma_{[\text{Ca}/\text{Fe}]} = 0.10, 0.11, \text{ and } 0.10$  for regions A, B, and C, respectively), indicating that the abundance spread of each region is smaller than or comparable to the estimated errors. We note that  $f_0$  converge between 0.10 and 0.20 for regions A and B, and  $< 0.10$  for region C.

The best models are shown in Figure 3 and the upper panels of Figure 4. The widths of the shaded areas correspond to  $\sigma_{[\text{X}/\text{Fe}]}$  and  $\sigma_{[\text{Fe}/\text{H}]}$  and the hatched areas correspond to  $1\sigma$  regions of the best-fit model (Equation (1)). Also shown in Figure 4 are low- $\alpha$  and high- $\alpha$  populations of Nissen & Schuster (2010, 2011). Note that we did not include region D in the following analysis, as it is not associated with main features in the  $E$ - $L_z$  plane.

Figure 4 confirms that our innermost halo and *Gaia* Enceladus stars correspond to the high-/low- $\alpha$  populations of Nissen & Schuster (2010), respectively. The general interpretation of the two populations is that the high- $\alpha$  population experienced more intense star formation prior to the onset of type Ia supernovae. To achieve such a high star formation rate at the early phase, the high- $\alpha$  population is usually considered to have formed in a massive galaxy, probably the Milky Way itself, although the detailed process is still under debate (e.g., Fernández-Alvar et al. 2018; Mackereth et al. 2019). On the other hand, the low- $\alpha$  population of Nissen & Schuster (2010) is now considered to be an accreted dwarf galaxy (*Gaia* Enceladus) from chemical abundances and kinematics (e.g., Belokurov et al. 2018; Haywood et al. 2018; Helmi et al. 2018).

Figure 4 also shows that the  $[\text{X}/\text{Fe}]$  ratios in high-energy retrograde halo stars are even lower for the two elements than the two halo populations in Nissen & Schuster (2010) at  $[\text{Fe}/\text{H}] \gtrsim -2$ . High-energy retrograde halo stars has been enriched only up to  $[\text{Fe}/\text{H}] \sim -2.5$  by the time of onset of type Ia supernovae, which indicates slow star formation.

The slow star formation indicated from the very low- $\alpha$  element abundances suggests inefficient star formation, which would suggest a low-mass progenitor. The mass ratio between the progenitor of high-energy retrograde halo stars and *Gaia* Enceladus was estimated by their metallicity distribution functions (Figure 2). The mean metallicity of *Gaia* Enceladus is  $\sim -1.3$ , and that of high-energy retrograde halo stars is  $\sim -1.6$ . The mass-metallicity relation of Kirby et al. (2013) for

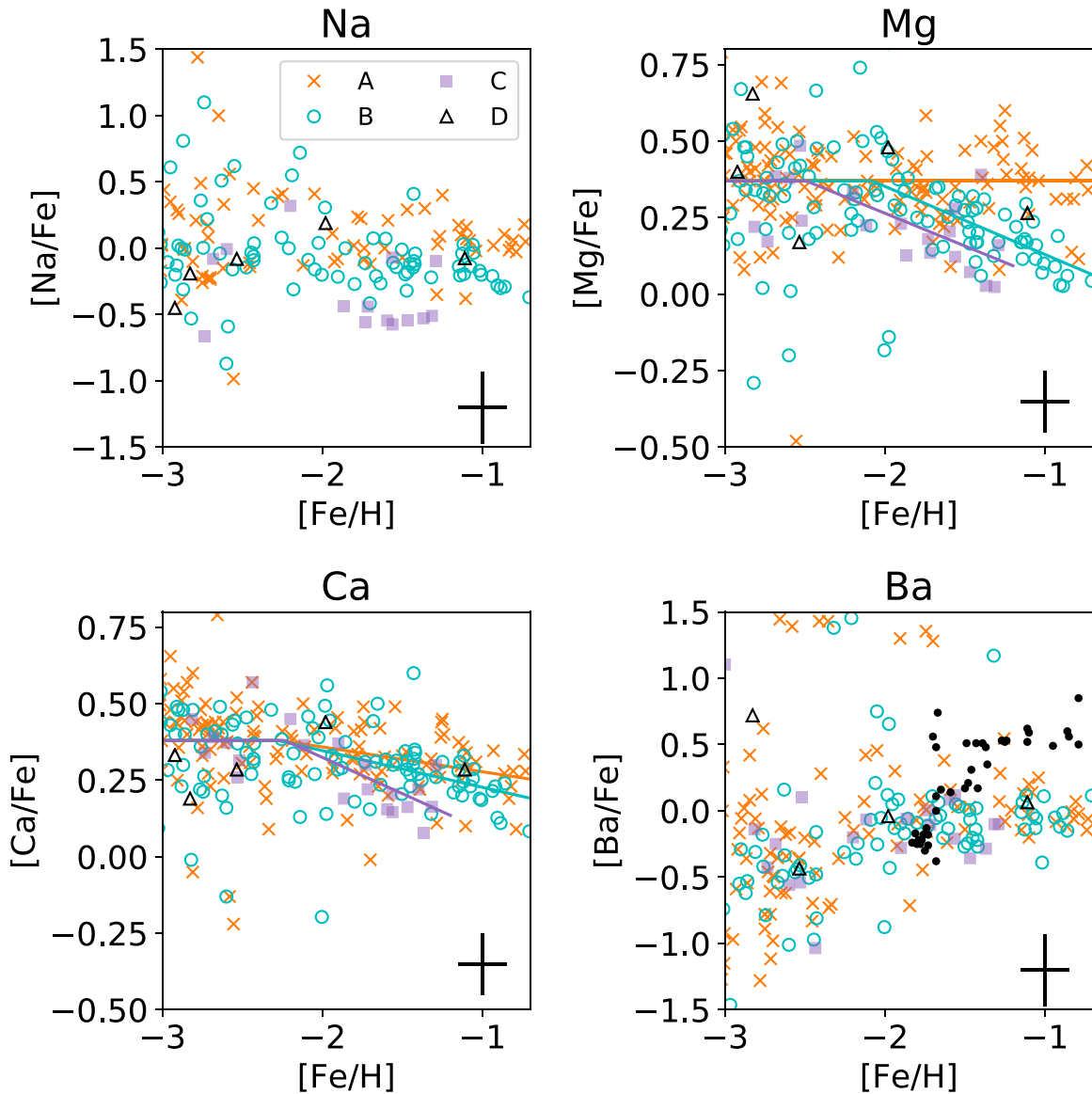


**Figure 3.** Chemical abundances of stars in the four regions for Na, Mg, Ca, and Ba. The data are taken from the SAGA database. The small black dots in the [Ba/Fe] panel are stars in  $\omega$  Cen from Norris & Da Costa (1995). Regions A–C appear to occupy different positions in each of the three panels for Na, Mg, and Ca. Note that the vertical scales for Na and Ba are different from the others. The lines in the Mg and Ca panels show the approximate chemical evolution of regions A–C. See Section 4 and Figure 4 for more details.

dwarf galaxies suggests that this 0.3 dex difference corresponds to a factor of  $\sim 10$  stellar mass difference.

Considering this large mass ratio, the impact of the accretion of the progenitor of high-energy retrograde halo stars to the Milky Way is likely to be much smaller than that of *Gaia* Enceladus. However, such a small system is still detectable by kinematics (Myeong et al. 2018c) and the addition of chemical abundance information brings us a robust conclusion and tells us the property of the progenitor. Note that we did not find many stars in the SAGA database that are similar in chemical abundances, but not in kinematics, to stars in high-energy retrograde halo stars. Therefore, high-energy retrograde halo stars would be a unique contributor to the Milky Way stellar halo.

Myeong et al. (2018d) discussed a possible connection of some of their high-energy retrograde substructures with  $\omega$  Centauri. The abundance pattern of high-energy retrograde halo stars is different from the stellar chemical abundances in the

globular cluster reported by Johnson & Pilachowski (2010); they reported almost flat  $\alpha$ -element abundances up to  $[\text{Fe}/\text{H}] \sim -1$  for  $\omega$  Centauri. This difference as well as the lack of Ba abundance anomalies (lower right panel of Figure 3) indicate that the majority of high-energy retrograde halo stars is unrelated to  $\omega$  Centauri.

Considering that we only used a compilation of past abundance measurements, which can be affected by systematic uncertainties, sufficient precision could be achieved in large spectroscopic surveys with a well-calibrated analysis if the surveys are designed well to study metal-poor stars. Indeed, we have reached a consistent conclusion for Mg using APOGEE DR14 data (Holtzman et al. 2015). However, other elements in APOGEE do not show as clear differences as Mg. This is due to the limitations of the current surveys in terms of the number of halo stars and the accuracy of chemical abundance measurements for metal-poor stars; additionally, it highlights

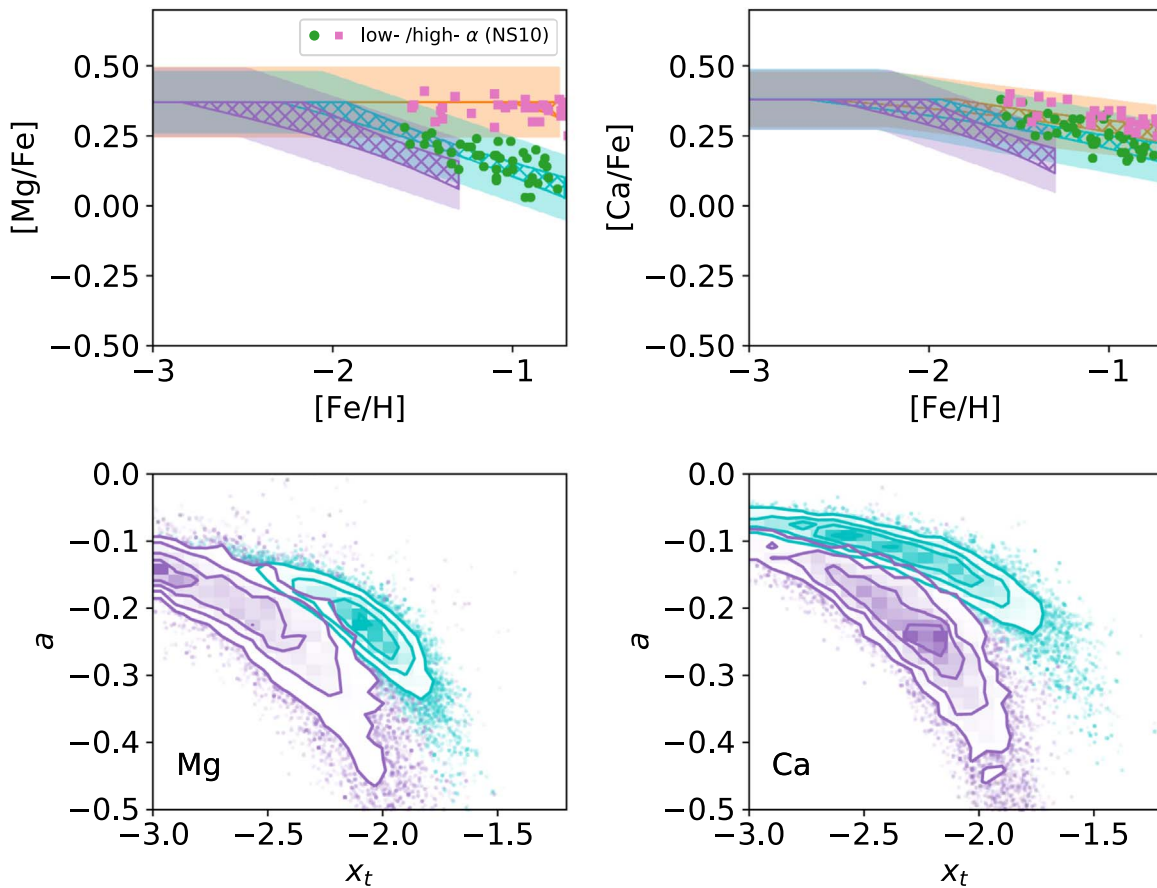


**Figure 4.** Upper panels: chemical abundance trends of stars in the three regions in the Milky Way halo for Mg and Ca. The colors for the three regions are the same as those in Figure 3. Halo stars from Nissen & (Schuster 2010, 2011; green/salmon symbols corresponding to low-/high- $\alpha$ ) are plotted for comparison purposes. Lower panels: posterior distributions of the obtained parameters for *Gaia* Enceladus and high-energy retrograde halo stars.  $x_t$  denotes the metallicity at which [Mg/Fe] or [Ca/Fe] starts decreasing, and  $a$  denotes the slope of the trend at [Fe/H] >  $x_t$  (see the text and Equations (1) and (4)).

the need for high-resolution spectroscopic surveys designed specifically to study halo stars.

### 5. Summary

Based on chemical abundances and kinematics from the SAGA database and *Gaia* DR2, we added new evidence that the excess of stars with highly retrograde orbits at high energy is caused by an accretion of a dwarf galaxy which is different from *Gaia* Enceladus/Sausage. Compared to previous studies that have pointed out or investigated the excess with stellar kinematics and metallicity (Helmi et al. 2017; Myeong et al. 2018c, 2018d), we included  $\alpha$ -element abundances in the investigation. The  $\alpha$ -element abundances are even lower than the low  $\alpha$ -element abundances of *Gaia* Enceladus, suggesting a different and lower mass progenitor. Although there are studies that pointed out that stars with large retrograde motion have low  $\alpha$ -element abundances (Stephens & Boesgaard 2002; Venn et al. 2004), these studies were in the pre-*Gaia* era, and hence our study is new in that it used the latest, most precise kinematics from the *Gaia* astrometric measurements and discussed the population in connection with a recently identified accretion signature in the Galaxy.

Our results are based on simple kinematic division. For a more detailed discussion, it is necessary to construct a pure sample for each component based on the abundance ratios. It would also be interesting to investigate the abundances of many elements for high-energy retrograde halo stars with high precision using high-quality spectra, for example, to include

neutron capture elements and compare them with stars in surviving dwarf galaxies around the Milky Way. These approaches are not yet feasible, due to the limited number of stars and the limited precision of abundances, as we used a compilation of past abundance measurements from the literature. We plan to carry out high-precision abundance analyses similar to those of Nissen & Schuster (2010) in the future.

We thank the referee for the detailed review of the paper. We thank Timothy C. Beers and Kohei Hattori for their helpful suggestions and comments. T.M. is supported by Grant-in-Aid for JSPS Fellows (grant No. 18J11326). W.A. and T.S. were supported by JSPS KAKENHI grant No. 16H02168, 16K05287, and 15HP7004. This work has made use of data from the European Space Agency (ESA) mission *Gaia* (<https://www.cosmos.esa.int/gaia>), processed by the *Gaia* Data Processing and Analysis Consortium (DPAC; <https://www.cosmos.esa.int/web/gaia/dpac/consortium>). Funding for the DPAC has been provided by national institutions, in particular the institutions participating in the *Gaia* Multilateral Agreement. This research has made use of the SAGA database (Suda et al. 2008).

### ORCID iDs

Tadafumi Matsuno <https://orcid.org/0000-0002-8077-4617>  
 Wako Aoki <https://orcid.org/0000-0002-8975-6829>  
 Takuma Suda <https://orcid.org/0000-0002-4318-8715>

## References

- Bailer-Jones, C. A. L., Rybizki, J., Fouesneau, M., Mantelet, G., & Andrae, R. 2018, *AJ*, **156**, 58
- Belokurov, V., Erkal, D., Evans, N. W., Koposov, S. E., & Deason, A. J. 2018, *MNRAS*, **478**, 611
- Belokurov, V., Zucker, D. B., Evans, N. W., et al. 2006, *ApJL*, **642**, L137
- Bernard, E. J., Ferguson, A. M. N., Schlafly, E. F., et al. 2016, *MNRAS*, **463**, 1759
- Bovy, J. 2015, *ApJS*, **216**, 29
- Carollo, D., Beers, T. C., Lee, Y. S., et al. 2007, *Natur*, **450**, 1020
- Chiba, M., & Beers, T. C. 2000, *AJ*, **119**, 2843
- Cui, X.-Q., Zhao, Y.-H., Chu, Y.-Q., et al. 2012, *RAA*, **12**, 1197
- Cutri, R. M., Skrutskie, M. F., van Dyk, S., et al. 2003, *yCat*, 2246
- Deason, A. J., Belokurov, V., Koposov, S. E., & Lancaster, L. 2018, *ApJL*, **862**, L1
- Fernández-Alvar, E., Fernández-Trincado, J. G., Moreno, E., et al. 2018, arXiv:1807.07269
- Gaia Collaboration, Brown, A. G. A., Vallenari, A., et al. 2016a, *A&A*, **595**, A2
- Gaia Collaboration, Brown, A. G. A., Vallenari, A., et al. 2018, *A&A*, **616**, A1
- Gaia Collaboration, Prusti, T., de Bruijne, J. H. J., et al. 2016b, *A&A*, **595**, A1
- Grillmair, C. J. 2006, *ApJL*, **645**, L37
- Haywood, M., Di Matteo, P., Lehnert, M. D., et al. 2018, *ApJ*, **863**, 113
- Helmi, A., Babusiaux, C., Koppelman, H. H., et al. 2018, *Natur*, **563**, 85
- Helmi, A., Veljanoski, J., Breddels, M. A., Tian, H., & Sales, L. V. 2017, *A&A*, **598**, A58
- Helmi, A., White, S. D. M., de Zeeuw, P. T., & Zhao, H. 1999, *Natur*, **402**, 53
- Holtzman, J. A., Shetrone, M., Johnson, J. A., et al. 2015, *AJ*, **150**, 148
- Ibata, R. A., Gilmore, G., & Irwin, M. J. 1994, *Natur*, **370**, 194
- Jean-Baptiste, I., Di Matteo, P., Haywood, M., et al. 2017, *A&A*, **604**, A106
- Johnson, C. I., & Pilachowski, C. A. 2010, *ApJ*, **722**, 1373
- Kirby, E. N., Cohen, J. G., Guhathakurta, P., et al. 2013, *ApJ*, **779**, 102
- Klement, R., Rix, H.-W., Flynn, C., et al. 2009, *ApJ*, **698**, 865
- Koppelman, H., Helmi, A., & Veljanoski, J. 2018, *ApJL*, **860**, L11
- Kruijssen, J. M. D., Pfeffer, J. L., Reina-Campos, M., Crain, R. A., & Bastian, N. 2018, *MNRAS*, in press
- Lindgren, L., Hernandez, J., Bombrun, A., et al. 2018, *A&A*, **616**, A2
- Mackereth, J. T., Schiavon, R. P., Pfeffer, J., et al. 2019, *MNRAS*, **483**, 3426
- Myeong, G. C., Evans, N. W., Belokurov, V., Amorisco, N. C., & Koposov, S. E. 2018a, *MNRAS*, **475**, 1537
- Myeong, G. C., Evans, N. W., Belokurov, V., Sanders, J. L., & Koposov, S. E. 2018b, *ApJ*, **863**, L28
- Myeong, G. C., Evans, N. W., Belokurov, V., Sanders, J. L., & Koposov, S. E. 2018c, *ApJL*, **856**, L26
- Myeong, G. C., Evans, N. W., Belokurov, V., Sanders, J. L., & Koposov, S. E. 2018d, *MNRAS*, **478**, 5449
- Nissen, P. E., & Schuster, W. J. 2010, *A&A*, **511**, L10
- Nissen, P. E., & Schuster, W. J. 2011, *A&A*, **530**, A15
- Norris, J. E., & Da Costa, G. S. 1995, *ApJ*, **447**, 680
- Smith, M. C., Evans, N. W., Belokurov, V., et al. 2009, *MNRAS*, **399**, 1223
- Stephens, A., & Boesgaard, A. M. 2002, *AJ*, **123**, 1647
- Suda, T., Hidaka, J., Aoki, W., et al. 2017, *PASJ*, **69**, 76
- Suda, T., Katsuta, Y., Yamada, S., et al. 2008, *PASJ*, **60**, 1159
- Suda, T., Yamada, S., Katsuta, Y., et al. 2011, *MNRAS*, **412**, 843
- Tolstoy, E., Hill, V., & Tosi, M. 2009, *ARA&A*, **47**, 371
- Venn, K. A., Irwin, M., Shetrone, M. D., et al. 2004, *AJ*, **128**, 1177
- Yamada, S., Suda, T., Komiya, Y., Aoki, W., & Fujimoto, M. Y. 2013, *MNRAS*, **436**, 1362